



## Ultrafast degradation of micropollutants in water *via* electro-periodate activation catalyzed by nanoconfined $\text{Fe}_2\text{O}_3$



Dongli Guo <sup>a</sup>, Yuan Yao <sup>b,\*</sup>, Shijie You <sup>c</sup>, Limin Jin <sup>a</sup>, Ping Lu <sup>d</sup>, Yanbiao Liu <sup>a,e, \*\*</sup>

<sup>a</sup> College of Environmental Science and Engineering, Textile Pollution Controlling Engineering Center of the Ministry of Ecology and Environment, Donghua University, Shanghai 201620, China

<sup>b</sup> MIIT Key Laboratory of Critical Materials Technology for New Energy Conversion and Storage, School of Chemistry and Chemical Engineering, Harbin Institute of Technology, Harbin 150080, China

<sup>c</sup> State Key Laboratory of Urban Water Resource and Environment, School of Environment, Harbin Institute of Technology, Harbin 150090, China

<sup>d</sup> Research Center for Analysis and Measurement, Donghua University, Shanghai 201620, China

<sup>e</sup> Shanghai Institute of Pollution Control and Ecological Security, 1239 Siping Road, Shanghai 200092, China

### ARTICLE INFO

#### Keywords:

Periodate activation  
Nanoconfinement effect  
Electrochemistry  
Singlet oxygen  
Water remediation

### ABSTRACT

Herein, we developed and evaluated an electrochemical periodate (PI) activation system for the ultrafast degradation of aqueous micropollutants ( $\tau < 3$  s). Filters constructed from carbon nanotubes (CNT) coated with  $\text{Fe}_2\text{O}_3$  nanoparticles on the outer ( $\text{Fe}_2\text{O}_3$ -out-CNT) and inner surfaces ( $\text{Fe}_2\text{O}_3$ -in-CNT) were prepared to regulate the generation of reactive oxygen species (ROS) during PI activation. The activation function of the electroactive nanohybrid filters lay in their ability to facilitate the redox cycling of  $\text{Fe}(\text{III})/\text{Fe}(\text{II})$  assisted by an electric field. The results showed that a non-radical (*i.e.*,  $^1\text{O}_2$ ) pathway dominated the degradation process in the electro/ $\text{Fe}_2\text{O}_3$ -in-CNT/PI system, while a contrastive radical pathway (*i.e.*,  $\text{HO}^\bullet$  and  $\text{IO}_3^\bullet$ ) was identified in the electro/ $\text{Fe}_2\text{O}_3$ -out-CNT/PI system. The electro/ $\text{Fe}_2\text{O}_3$ -in-CNT/PI system exhibited enhanced catalytic activity towards the micropollutants degradation relative to its electro/ $\text{Fe}_2\text{O}_3$ -out-CNT/PI counterpart. Density functional theory calculations suggested that PI could be directly decomposed under the nanoconfined environment, rather than forming a stable adsorption complex in the unconfined system.

### 1. Introduction

Growing concern for micropollutants is gained due to their potential negative effects on aquatic ecosystem and human health [1–3]. However, conventional wastewater treatment technologies such as biological degradation, physical adsorption, and chemical oxidation failed to decontaminate these micropollutants due to limitations associated with sluggish reaction kinetics, poor stability and/or limited selectivity [4–6]. It is, therefore, imperative to seek advanced and innovative strategies to eliminate these micropollutants from water.

Recently, periodate (PI,  $\text{IO}_4^-$ )-based advanced oxidation processes have attracted widespread interest for wastewater treatment and protection of the aquatic environment from micropollutants [7–9]. Like other oxyanions, such as hydrogen peroxide ( $\text{H}_2\text{O}_2$ ), peroxymonosulfate (PMS), and peroxydisulfate (PDS), the reactivity of PI towards organic

molecule is rather limited ( $E^\theta = 1.6$  V) [10–14]. Therefore, various strategies (*e.g.*, UV irradiation, ultrasound, alkali, hydroxylamine, and transition metals) have been adopted to activate PI into more reactive intermediates (*e.g.*,  $\text{HO}^\bullet$ ,  $\text{IO}_3^\bullet$ ,  $\text{O}_2^\bullet$ , and  $^1\text{O}_2$ ) *via* radical and/or non-radical pathways [8,9,15–17]. Among these, considerable efforts have been devoted to the use of transition metal-based heterogeneous catalysts due to their abundance and cost-effectiveness [18–20]. For example, Zong et al. [21] reported that PI can be effectively activated by nano zero-valent iron, leading to enhanced organic degradation performance. However, their relatively low activation efficiency and poor stability remains a challenge due to poor mass transport kinetics in conventional batch reactor as well as potential dissolution of transition metal ions into water [22,23].

To encapsulate those transition metal catalysts into a nanoconfined environment may provide a viable solution to address these

\* Corresponding author.

\*\* Corresponding author at: College of Environmental Science and Engineering, Textile Pollution Controlling Engineering Center of the Ministry of Ecology and Environment, Donghua University, Shanghai 201620, China.

E-mail addresses: [yyuan@hit.edu.cn](mailto:yyuan@hit.edu.cn) (Y. Yao), [yanbiaoliu@dhu.edu.cn](mailto:yanbiaoliu@dhu.edu.cn) (Y. Liu).

aforementioned limitations. A previous study reported that  $\text{Fe}_2\text{O}_3$  catalysts confined within carbon nanotubes (CNT) showed a remarkably faster kinetic when compared with a nonconfined counterpart (with  $\text{Fe}_2\text{O}_3$  loaded onto the outer surface of CNT) toward  $\text{H}_2\text{O}_2$  activation [24], yet their application is significantly hindered by the challenges associated with their post-separation from the reaction solution. An electrochemical CNT filter functionalized with nanoconfined  $\text{Fe}_2\text{O}_3$  bring this concept one step further by not only eliminates the necessity of catalyst recovery, but also enables a continuous-flow operation. We previously demonstrated that an electroactive nanohybrid filter, composed of CNT and  $\text{Fe}_2\text{O}_3$ , could trigger electro-Fenton reactions with tunable radical species [25]. Interestingly, for the system with the  $\text{Fe}_2\text{O}_3$  coating confined within CNT (*i.e.*,  $\text{Fe}_2\text{O}_3$ -in-CNT) filter, the dominant reactive species was identified as  $^1\text{O}_2$ , while that with  $\text{Fe}_2\text{O}_3$  loaded onto CNT external sidewalls ( $\text{Fe}_2\text{O}_3$ -out-CNT) was  $\text{HO}^\bullet$ . One clear advantage of this nanohybrid filter was the adoption of a convection-enhanced mass transport flow-through configuration [26]. Another advantage was the high selectivity of  $^1\text{O}_2$  toward electron-rich substances as well as longer lifetime than  $\text{HO}^\bullet$  (2  $\mu\text{s}$  vs 20 ns) [27]. In addition, the cycling of  $\text{Fe}(\text{III})/\text{Fe}(\text{II})$  couple and system stability could be improved greatly by exerting an external electric field. The working pH could also be extended from acidic to weakly alkaline conditions thanks to the enhanced catalyst stability. Due to the chemical similarities between  $\text{H}_2\text{O}_2$  and PI, it is reasonable to hypothesize that PI could be also activated by the nanohybrid filter.

The objectives of this study were as follow: 1) develop and evaluate an electrochemical filtration system for efficient PI activation; 2) compare the PI activation performance under confined and unconfined systems from the degradation of representative micropollutants; 3) determine (by experiment/theoretical calculation) the underlying mechanism of the proposed technology and identify the synergistic effects between the electric field, flow-through design, and confined catalysis; 4) examine the practical applicability of the proposed technology. To the best of our knowledge, this is the first attempt to achieve ultrafast degradation of micropollutants using electrochemical PI activation. This study provides a novel design based on an electrochemistry-mediated PI activation system with tunable oxidation pathways in a practical continuous-flow configuration.

## 2. Materials and methods

### 2.1. Materials

Potassium periodate ( $\text{KIO}_4$ , 99.8%), bisphenol A (BPA, >99.8%), sulfamethoxazole (SMX, 98.0%), 2,4,6-trichlorophenol (2,4,6-TCP, 98.0%), deuterium oxide ( $\text{D}_2\text{O}$ , 99.9%), L-histidine ( $\geq 99.0\%$ ), 2,2,6,6-tetramethylpiperidine (TEMP,  $\geq 98.0\%$ ), 5,5-dimethyl-1-pyrrolidine-N-oxide (DMPO, 97.0%), and methyl phenyl sulfoxide (PMSO, >98.0%) were obtained from Shanghai Aladdin Biological Technology Co., Ltd. (Shanghai, China). Iron nitrate ( $\text{Fe}(\text{NO}_3)_3 \cdot 9\text{H}_2\text{O}$ ,  $\geq 98.0\%$ ), nitric acid ( $\text{HNO}_3$ , 65.0–68.0%), sodium hydroxide ( $\text{NaOH}$ ,  $\geq 96.0\%$ ), potassium phosphate ( $\text{KH}_2\text{PO}_4$ ,  $\geq 98.0\%$ ), sodium chloride ( $\text{NaCl}$ ,  $\geq 98.0\%$ ), sodium sulfate ( $\text{Na}_2\text{SO}_4$ ,  $\geq 99.0\%$ ), sodium nitrate ( $\text{NaNO}_3$ ,  $\geq 98.5\%$ ), methylene blue (MB), phenol, levofloxacin (LFX), furfuryl alcohol (FFA,  $\geq 98.5\%$ ), *tert*-butyl alcohol (TBA,  $\geq 98.0\%$ ), *p*-benzoquinone (*p*-BQ,  $\geq 98.0\%$ ), tetracycline (TC,  $\geq 98.0\%$ ), and ethanol ( $\geq 96.0\%$ ) were purchased from Sinopharm Chemical Reagent Co. Ltd. (Shanghai, China). Methanol ( $\geq 99.9\%$ ), phosphoric acid, formic acid and acetonitrile ( $\geq 99.9\%$ , chromatographic grade) were from Titan Scientific Co., Ltd. (Shanghai, China). Multiwalled CNT (diameter, 10–20 nm, length, 0.5–2.0  $\mu\text{m}$ ) were supplied by Nanjing XFNANO Materials Tech Co., Ltd. (Nanjing, China). Ultrapure water (resistivity  $\geq 18.2\text{ M}\Omega\text{ cm}$ ) was used in all experiments.

### 2.2. Experimental setup and procedures

$\text{Fe}_2\text{O}_3$  in/out CNT (denoted as  $\text{Fe}_2\text{O}_3$ -in-CNT and  $\text{Fe}_2\text{O}_3$ -out-CNT, respectively) hybrid filters were prepared according previous procedures with minor modifications [24,25,28]. The preparation procedure is given in Text S1.

Electrochemical filtration experiments were performed at  $25 \pm 1^\circ\text{C}$  in an electrochemistry-modified Whatman polycarbonate filtration casing (Fig. S1). Two operational modes (*i.e.*, single-pass filtration and batch) were performed for comparison. The hybrid filter was operated cathodically and was electrically connected *via* a Ti ring and rod to the DH1766A-1 high precision DC power supply (Beijing, China). A perforated Ti sheet was operated as anode. A ISM833C peristaltic pump (Ismatec, Switzerland) was used to control the flow rate. Prior to the degradation experiments, filters were first adsorption saturated by passing a solution of BPA (180 mL of 0.022 mM) through the device for 2 h. For the electrochemical filtration experiments, BPA feed solution (50 mL of 0.022 mM) and PI (2.0 mM) were passed through the flow-through reactor (Fig. S2). For the batch mode, the hybrid filter cathode and Ti sheet anode were put into a glass reactor containing 50 mL of 0.022 mM BPA and 2.0 mM PI solution at  $-1.5\text{ V}$ . The role of dissolved oxygen was investigated by pre-purging the BPA solution with  $\text{N}_2$  before passing through the reactor. Solution pH was adjusted using HCl or NaOH (1.0 mM each). Aqueous samples (1.0 mL) from each experiment were then collected periodically and filtered (0.22  $\mu\text{m}$  polyester membrane filter) prior to analysis (see below). All experiments were conducted in triplicate to ensure reproducibility.

### 2.3. Analytical methods

The concentrations of BPA, 2,4,6-TCP, TC, LFX, phenol, SMX, FFA,  $\text{IO}_4^-$ , and  $\text{IO}_3^-$  were determined by HPLC with variable wavelength detector (VWD) detection following separation on a COSMOSIL 5 C-18-MSII column (Nacalai Tesque, Kyoto, Japan) using an Alliance 2695 Separation Module (Waters, USA). Detailed operational parameters are given in Table S1. BPA degradation intermediates were identified by liquid chromatography-mass spectrometry (LC-MS) using a LC1290 infinity-6470 LC-MS system (Agilent, Singapore). The concentration of MB was measured by a UV-vis spectrometry ( $\lambda_{\text{max}} = 665\text{ nm}$ ) on a UV2600 spectrophotometer (Shimadzu, Japan). The concentrations of leaching Fe ions were measured by inductively coupled plasma mass spectrometry (ICP-MS) using an iCAP<sup>TM</sup> Q (Thermo Scientific, USA). Reactive species were identified by quenching experiments, using TBA, FFA, *p*-BQ, or PMSO as the scavenging agent, and by electron paramagnetic resonance (EPR) with an EMXnano spectrometer (Bruker, Beijing, China) using DMPO or TEMP as the spin-trapping agent.

### 2.4. Theoretical calculations

The density functional theory (DFT) calculations were performed by using the Gaussian 09 program [29]. B3LYP was employed with the 6-31G(d) basis set to treat O, C, and H elements. The LANL2DZ basis set was used to treat Fe and I. A (6,6) CNT model with five cell replication units was constructed, in which all boundary C atoms were saturated by H atoms. A Fe-O unit was used to mimic the  $\text{Fe}_2\text{O}_3$ .

## 3. Results and discussion

### 3.1. Characterization of confined and unconfined nanohybrid filters

The  $\text{Fe}_2\text{O}_3$ -in-CNT and  $\text{Fe}_2\text{O}_3$ -out-CNT samples were synthesized *via* a wet chemistry method [24,30]. Due to the presence of oxygen containing groups (*e.g.*, carbonyl groups), CNT are enable to adsorb  $\text{Fe}^{3+}$  from the acetone/ $\text{Fe}(\text{NO}_3)_3 \cdot 9\text{H}_2\text{O}$  solution *via* electrostatic force [31–33]. Then,  $\text{Fe}_2\text{O}_3$  nanoparticles could be *in-situ* formed within the channel or on the outer sidewall of CNT afterward the ultrasonic,

stirring and calcination treatment (see *Text S1* for the detailed preparation procedure). The morphology of CNT after pre-oxidation treatment was first examined by transmission electron microscopy (TEM). The images showed that the CNT with closed tips and open tips were obtained (*Fig. S3*). Representative high-angle annular dark-field scanning TEM images suggested that the  $\text{Fe}_2\text{O}_3$  nanoparticles were randomly distributed within the CNT channels of the  $\text{Fe}_2\text{O}_3$ -in-CNT (*Fig. 1(a)*) and on the outer CNT sidewalls of the  $\text{Fe}_2\text{O}_3$ -out-CNT (*Fig. 1(b)*). These results demonstrated that the location of the  $\text{Fe}_2\text{O}_3$  nanoparticles could be regulated by tailoring the CNT pre-oxidation conditions as well as the subsequent wet chemistry parameters during the fabrication process.

Mössbauer spectroscopy was employed to examine the valence state and coordination environment of iron (*Text S2*). The  $^{57}\text{Fe}$  Mössbauer spectra (*Fig. 1(c), (d)*) and corresponding fitting parameters (*Table S2*) suggest the sole presence of  $\text{Fe}^{3+}$  species on both  $\text{Fe}_2\text{O}_3$ -in-CNT and  $\text{Fe}_2\text{O}_3$ -out-CNT samples [34]. Moreover, the Mössbauer spectroscopy measurements provide an insight into the coordination environment of Fe in both samples. Two peaks with different electrical quadrupole splitting (QS) values (0.53 mm/s and 0.96 mm/s), corresponding to  $\text{Fe}^{3+}$  in octahedral and tetrahedral coordination sites were observed in the  $\text{Fe}_2\text{O}_3$ -in-CNT (*Fig. 1(c)*). Nevertheless, only  $\text{Fe}^{3+}$  in an octahedral coordination site exists in the  $\text{Fe}_2\text{O}_3$ -out-CNT (*Fig. 1(d)*), which might be due to the curvature of the graphene sheets in CNT, the corresponding coordination of Fe is different between the concave and convex surfaces of CNT [35]. Moreover, the crystal structure and electronic properties of  $\text{Fe}_2\text{O}_3$ -in/out-CNT filters were further investigated by X-ray diffraction (XRD) and X-ray photoelectron spectroscopy (XPS). The XRD patterns

show that both  $\text{Fe}_2\text{O}_3$ -out-CNT and  $\text{Fe}_2\text{O}_3$ -in-CNT exhibit similar diffraction peaks at  $35.6^\circ$ ,  $43.3^\circ$ , and  $53.7^\circ$ , corresponding to the (311), (400), and (422) facets of  $\text{Fe}_2\text{O}_3$  (PDF#39-1346, *Fig. S4*). High-resolution XPS confirmed the presence of  $\text{Fe} 2p$ ,  $\text{C} 1s$ , and  $\text{O} 1s$  in both samples. As observed in *Fig. S5*, the  $\text{Fe} 2p$  peak of  $\text{Fe}_2\text{O}_3$ -in-CNT was much weaker than that of  $\text{Fe}_2\text{O}_3$ -out-CNT despite their similar Fe contents, probably due to the limited probe depth of the photoelectrons (3–5 nm) for the detection of  $\text{Fe}_2\text{O}_3$  inside the CNT [24]. The  $\text{C} 1s$  spectra (*Fig. S6(a)*) can be deconvoluted into three peaks centered at 291.0 eV, 287.1 eV, and 284.9 eV, associated with  $\pi \rightarrow \pi^*$  transition of carbon atoms of graphene structures,  $\text{C}=\text{O}$  bond, and  $\text{sp}^3 \text{C}-\text{C}$  bonds of graphitic carbon, respectively. The  $\text{O} 1s$  spectra (*Fig. S6(b)*) could be deconvoluted into  $\text{R-OH}$  (532.0 eV, surface hydroxyl groups),  $-\text{COOH}$  (533.6 eV, oxygen in esters and anhydrides) in CNT, and a  $\text{Fe}-\text{O}$  peak (530.0 eV,  $-\text{FeO}_x$  group). All the results demonstrated that we have successfully fabricated the  $\text{Fe}_2\text{O}_3$ -out-CNT and  $\text{Fe}_2\text{O}_3$ -in-CNT hybrid filters.

### 3.2. Electrochemical periodate activation for micropollutant degradation

BPA was chosen as a model refractory micropollutant to evaluate the efficacy of electrochemical PI activation system. *Fig. 2* shows that there was insignificant degradation of BPA with PI alone (1.2%), and no significant improvement was observed for BPA degradation after applying an electric field (E/PI). This excluded the role of the electric field in PI activation. Control experiments using CNT alone led to inappreciable BPA removal as well (1.1%). Furthermore, comparative experiments

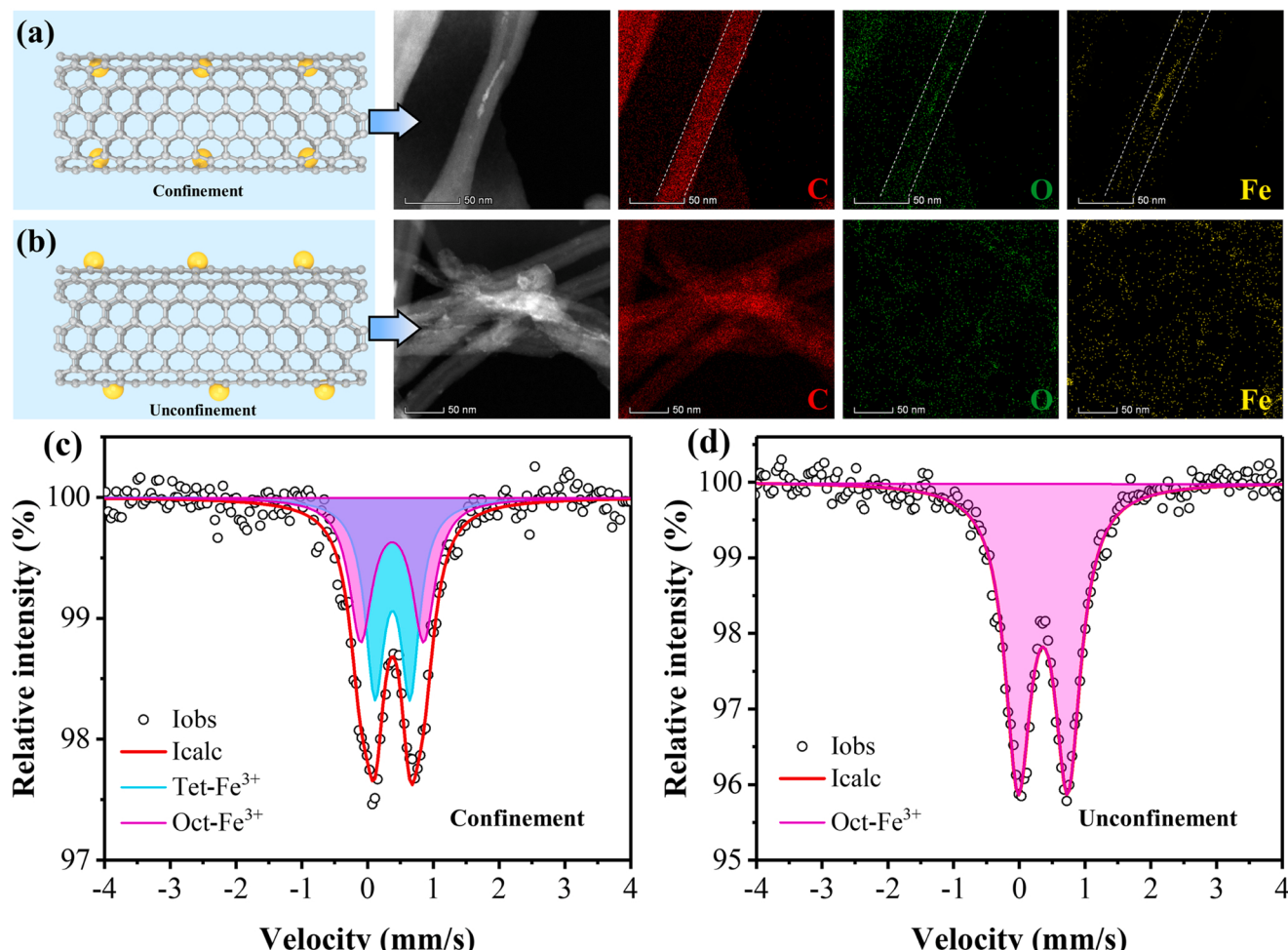


**Fig. 1.** Illustration of (a)  $\text{Fe}_2\text{O}_3$ -in-CNT filter and (b)  $\text{Fe}_2\text{O}_3$ -out-CNT filter, and the corresponding HADDF-STEM and EDX elemental mappings.  $^{57}\text{Fe}$  Mössbauer spectra of (c)  $\text{Fe}_2\text{O}_3$ -in-CNT and (d)  $\text{Fe}_2\text{O}_3$ -out-CNT recorded at room temperature.

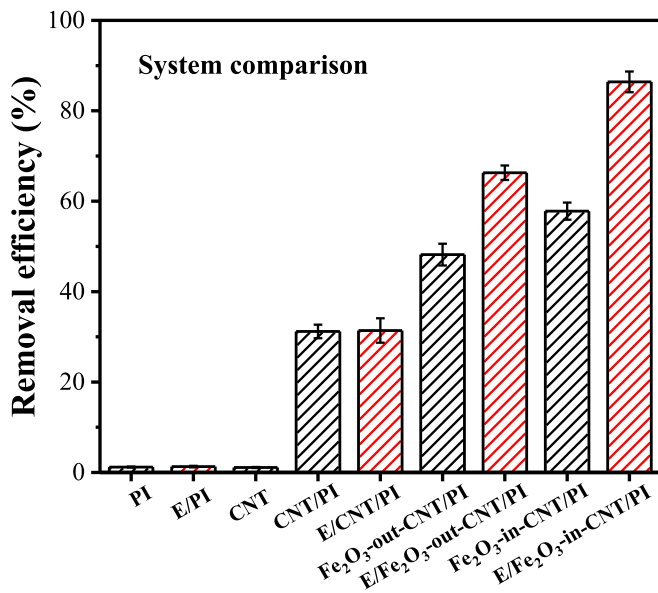


**Fig. 2.** Degradation of BPA in different systems. Experimental conditions:  $[BPA]_0 = 0.022 \text{ mM}$ , voltage =  $-1.0 \text{ V}$ ,  $[PI]_0 = 1.0 \text{ mM}$ , flow rate =  $1.0 \text{ mL/min}$ , and  $[pH]_0 = 5.7$ .

showed that CNT/PI and electro(E)/CNT/PI exhibited similar BPA removal efficiencies (31.2% and 31.4%), thereby the role of the electric field was further excluded. In contrast, the removal efficiency of BPA was appreciably enhanced in the  $\text{Fe}_2\text{O}_3$ -in-CNT/PI and  $\text{Fe}_2\text{O}_3$ -out-CNT/PI systems, which could be attributed to the enhanced cycling of Fe(III)/Fe(II) pairs by the applied electric field. Interestingly, the E/Fe<sub>2</sub>O<sub>3</sub>-in-CNT/PI system achieved the BPA degradation efficiency as high as 86.4%, a value being approximately 1.3 times of that for E/Fe<sub>2</sub>O<sub>3</sub>-out-CNT/PI one (66.3%). The significantly enhanced catalytic activity of the E/Fe<sub>2</sub>O<sub>3</sub>-in-CNT/PI system might be due to a strong electronic interaction between  $\text{Fe}_2\text{O}_3$  and the CNT interior surface, which accelerates electron transfer from the  $\text{Fe}_2\text{O}_3$  nanoparticles to the carbon shell [23, 24, 36]. The performance of  $\text{Fe}_2\text{O}_3/\text{PI}$  (51.0%) and E/Fe<sub>2</sub>O<sub>3</sub>/PI (53.2%) is much less than that of E/Fe<sub>2</sub>O<sub>3</sub>-in-CNT/PI system (86.4%), indicating the indispensable role of CNT (Fig. S7).



Applied voltage played an essential role in the electrochemical treatment process. As indicated in Fig. 3(a), degradation efficiency increased from 64.4% to 91.7% as the applied voltage was declined from  $-0.5 \text{ V}$  to  $-1.5 \text{ V}$  in the E/Fe<sub>2</sub>O<sub>3</sub>-in-CNT/PI system. No improvement in degradation was observed with further reductions in the applied voltage of  $-2.0 \text{ V}$ , indicating the occurrence of side reactions (Eqs. (1)–(3)). The  $\text{Fe}(\text{OH})_3$  generated resulted in the generation of iron sludge which

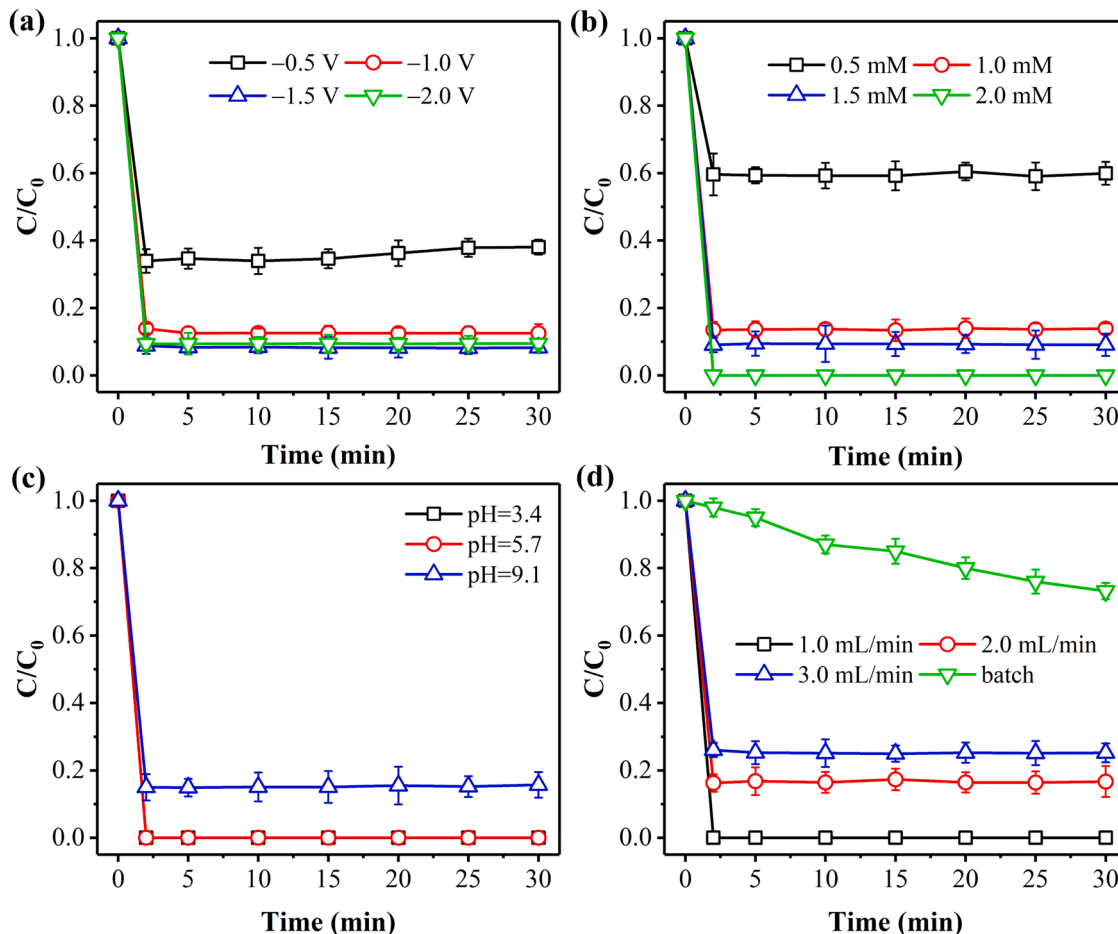


**Fig. 3.** Effect of (a) applied voltage, (b) PI concentration, (c) solution pH, and (d) flow rate on the degradation of BPA in the E/Fe<sub>2</sub>O<sub>3</sub>-in-CNT/PI. Experimental conditions:  $[BPA]_0 = 0.022 \text{ mM}$ .

decreased the decomposition efficiency of PI. Fig. 3(b) shows the impact of PI concentration on BPA removal in the E/Fe<sub>2</sub>O<sub>3</sub>-in-CNT/PI system. The removal efficiency of BPA was increased from 40.5% (0.5 mM PI) to 100% (2.0 mM PI), suggesting that the production of ROS increased with increasing PI concentration. Additionally, the solution pH also had a significant impact on the oxidative capability of PI and the removal efficiency of BPA. The removal efficiency of BPA decreased from 100% to 84.8% as the solution pH increased from 3.4 to 9.1 (Fig. 3(c)). The relatively high pH tolerance of the E/Fe<sub>2</sub>O<sub>3</sub>-in-CNT/PI degradation system (84.8% degradation at pH 9.1) represented a significant improvement in performance compared with traditional homogeneous Fe-based PI-activation systems which showed significant performance reductions at pH > 3.0 [7]. The effects of flow rate on BPA removal efficiency are shown in Fig. 3(d). As the flow rate increased from 1.0 to 3.0 mL/min, BPA removal efficiency decreased from 100% to 74.6%. This was mainly due to the reduced residence time and contact between reactants and active sites at the higher flow rates. Noticeably, when compared with a conventional batch reactor (26.8% in 30 min), the flow-through configuration demonstrated a 3.7-fold increase in BPA degradation efficiency by virtue of the convection-enhanced mass transport.

The efficacy of the E/Fe<sub>2</sub>O<sub>3</sub>-in-CNT/PI system towards the degradation of other organic pollutants, *e.g.*, LFX, MB, SMX, TC, and 2,4,6-TCP was also evaluated. Fig. S8 shows that under the same conditions of operation, the degradation efficiencies of these additional pollutants were > 85.0% under the single-pass mode. The effect of different oxidants (*i.e.*, H<sub>2</sub>O<sub>2</sub>, PDS, and PMS) on BPA removal efficiency was also

investigated. Fig. S9(a) reveals that the BPA removal efficiencies follow the decreasing order of E/Fe<sub>2</sub>O<sub>3</sub>-in-CNT/PI (100%) > E/Fe<sub>2</sub>O<sub>3</sub>-in-CNT/PMS (96.3%) > E/Fe<sub>2</sub>O<sub>3</sub>-in-CNT/PDS (56.7%) > E/Fe<sub>2</sub>O<sub>3</sub>-in-CNT/H<sub>2</sub>O<sub>2</sub> (39.3%). Although the E/Fe<sub>2</sub>O<sub>3</sub>-in-CNT/PMS system also exhibited excellent initial high degradation performance (>90%), its long-term efficiency decreased by 46.5% after 48 h continuous operation, thus limiting its practical application (Fig. S9(b)). Hence, the E/Fe<sub>2</sub>O<sub>3</sub>-in-CNT/PI system might be a promising and effective alternative advanced oxidation process for wastewater remediation.

### 3.3. Mechanistic insights

The essential ROS responsible for organic degradation in the E/Fe<sub>2</sub>O<sub>3</sub>-in-CNT/PI and E/Fe<sub>2</sub>O<sub>3</sub>-out-CNT/PI systems were identified using quenching experiments and EPR analysis. TBA was used as the scavenger for HO<sup>•</sup> ( $k = (3.8\text{--}7.6) \times 10^8 \text{ mol}^{-1} \text{ s}^{-1}$ ) [8]. FFA and PMSO were the scavengers for <sup>1</sup>O<sub>2</sub> ( $k = 1.2 \times 10^8 \text{ mol}^{-1} \text{ s}^{-1}$ ) [37] and high-valence Fe-oxo species, respectively. In addition, *p*-BQ was employed as scavenger for O<sub>2</sub><sup>•-</sup> ( $k = (0.90\text{--}1.00) \times 10^9 \text{ mol}^{-1} \text{ s}^{-1}$ ) [38]. As shown in Fig. 4(a), the addition of TBA and PMSO showed limited inhibition on BPA degradation in the E/Fe<sub>2</sub>O<sub>3</sub>-in-CNT/PI system. In contrast, the addition of FFA (100 mM) almost completely inhibited the BPA degradation (to 3.5%), indicating <sup>1</sup>O<sub>2</sub> was the dominant ROS. Furthermore, the presence of L-histidine (another <sup>1</sup>O<sub>2</sub> scavenger [39]) similarly hindered the BPA removal performance (Fig. S10). Considering FFA or L-histidine could be directly consumed by PI, control experiments between PI (2.0 mM) and FFA (100 mM) or L-histidine (100 mM) were

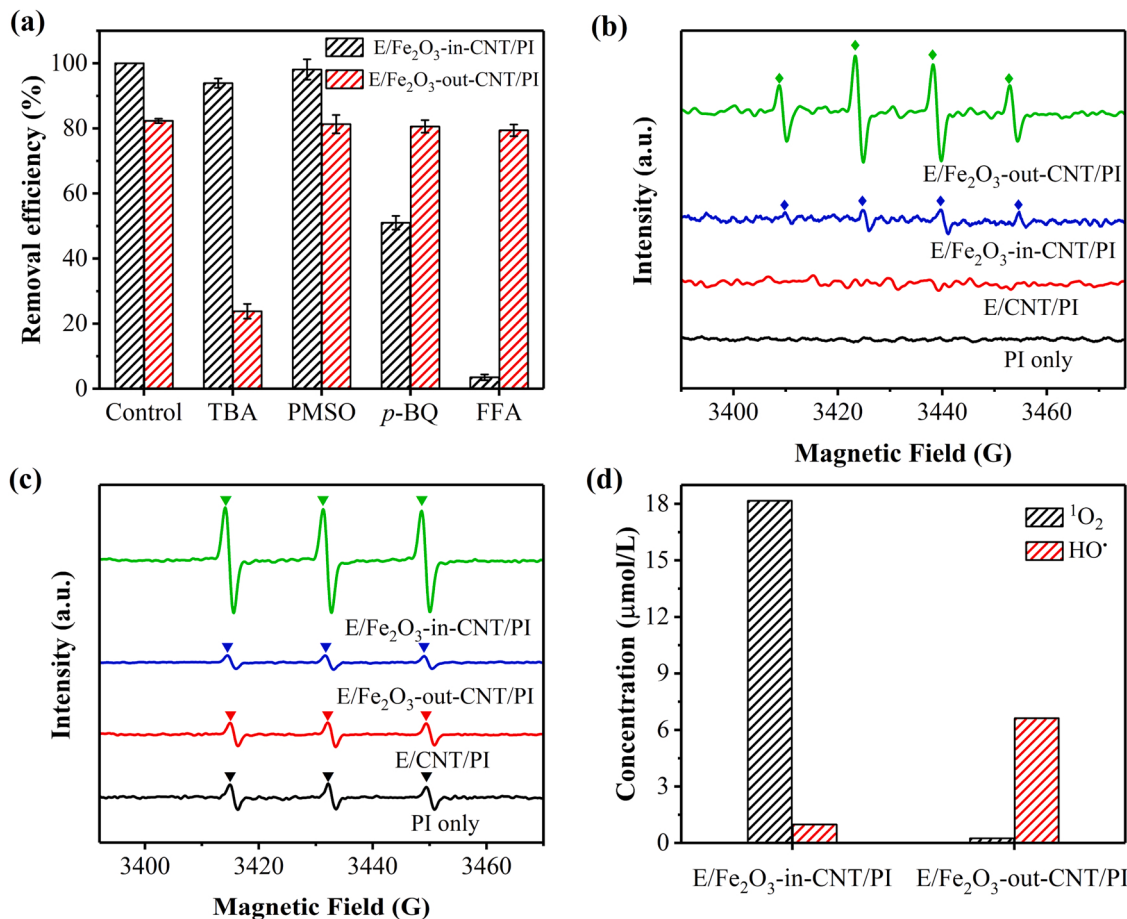
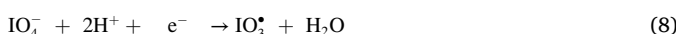
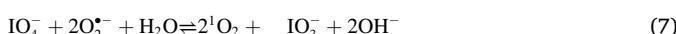
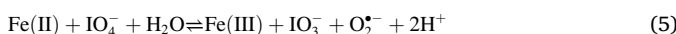
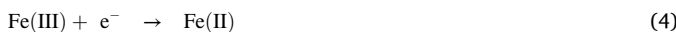


**Fig. 4.** Identification of reactive oxidizing species: (a) quenching tests with different radical scavengers. (b) EPR characterization using DMPO in the absence of BPA. (c) EPR characterization using TEMP in the absence of BPA. (d) quantitative determination of <sup>1</sup>O<sub>2</sub> and HO<sup>•</sup>, respectively. Experimental conditions: [TBA]<sub>0</sub> = 100 mM, [FFA]<sub>0</sub> = 100 mM or 1.0 mM, [*p*-BQ]<sub>0</sub> = 50 mM, [PMSO]<sub>0</sub> = 5.0 mM, [DMPO]<sub>0</sub> = [TEMP]<sub>0</sub> = 50 mM, [BPA]<sub>0</sub> = 0.022 mM, [PI]<sub>0</sub> = 2.0 mM, [pH]<sub>0</sub> = 5.7, voltage = -1.5 V, and flow rate = 1.0 mL/min.

further performed. As shown in Fig. S11 and S12, the interaction between FFA (or L-histidine) and PI was rather negligible, indicating the inability of PI to be oxidized by FFA or L-histidine [8,15,40]. Thus, the inhibition of BPA degradation kinetics was mainly originated from the scavenging of  $^1\text{O}_2$  [41]. Thereby, it fully proved that  $^1\text{O}_2$  was the main ROS in the E/Fe<sub>2</sub>O<sub>3</sub>-in-CNT/PI system. The addition of *p*-BQ partially suppressed BPA degradation to 51.0%, indicating the possible contribution of  $\text{O}_2^{\bullet-}$  to BPA degradation (Eqs. (4) and (5)). However, the negligible degradation of BPA by  $\text{O}_2^{\bullet-}$  was probably due to its mild oxidative capability (Fig. S13), indicating that it might be a key intermediate in  $^1\text{O}_2$  generation during PI activation. The *in situ* generated  $\text{O}_2^{\bullet-}$  could then recombine to form  $^1\text{O}_2$  (Eq. (6)). Besides, the direct oxidation of  $\text{O}_2^{\bullet-}$  to  $^1\text{O}_2$  by residual PI is also a thermodynamically possible alternate pathway (Eq. (7)).



In the E/Fe<sub>2</sub>O<sub>3</sub>-out-CNT/PI system, the introduction of TBA inhibited the degradation of BPA by 58.5%, highlighting the significant contribution from HO<sup>•</sup> toward the BPA degradation. While the presence of FFA (1.0 mM), PMSO (5.0 mM) and *p*-BQ (50 mM) demonstrated negligible inhibition on the BPA elimination, further ruling out the involvement of  $^1\text{O}_2$ , high-valence Fe-oxo species, and  $\text{O}_2^{\bullet-}$  to the BPA degradation process. It should be noted that FFA, *p*-BQ or PMSO could also be oxidized by HO<sup>•</sup> due to its non-selectivity. However, the addition of FFA (or *p*-BQ, PMSO) in the E/Fe<sub>2</sub>O<sub>3</sub>-out-CNT/PI system showed limited suppression on the BPA degradation kinetics. It has been previously reported that low concentration of FFA (<10 mM) may not react with HO<sup>•</sup> due to mass transport limitations [42]. Although *p*-BQ could react with HO<sup>•</sup> to suppress the BPA degradation, it also assumed a role as electron shutter to accelerate the Fe(III)/Fe(II) cycle and to promote BPA degradation simultaneously [43]. These two concurrent processes may not significantly change the overall BPA degradation kinetics. While the interaction between HO<sup>•</sup> and PMSO may lead to the generation of  $[\text{Fe}^{\text{IV}}\text{O}]^{2+}$  and/or  $\equiv\text{Fe}^{\text{III}}(\text{O}_2\text{H})$ , which might be responsible for the subsequent degradation of BPA [44]. Furthermore, a BPA degradation of 23.8% could still be observed in the presence of excessive TBA (100 mM), possibly resulting from the generation of  $\text{IO}_3^{\bullet}$  in the E/Fe<sub>2</sub>O<sub>3</sub>-out-CNT/PI system.

Although a conclusive method for the detection of  $\text{IO}_3^{\bullet}$  is still unavailable, the possible generation of  $\text{IO}_3^{\bullet}$  could be indirectly verified via scavenging experiments and the degradation of selected pollutants [16, 21,45]. For example, it has been reported that the  $\text{IO}_3^{\bullet}$  was unreactive towards 2,4,6-TCP [45]. Under test, 2,4,6-TCP was effectively degraded (97.8%) in the E/Fe<sub>2</sub>O<sub>3</sub>-in-CNT/PI system suggesting that a contribution from  $\text{IO}_3^{\bullet}$  could be ignored (Fig. S8). The contribution of  $\text{IO}_3^{\bullet}$  to degradation of pollutants in the E/Fe<sub>2</sub>O<sub>3</sub>-out-CNT/PI system was also investigated using phenol, SMX, and 2,4,6-TCP. The results given in Fig. S14 show that phenol (97.4%) and SMX (87.6%) were efficiently degraded in the E/Fe<sub>2</sub>O<sub>3</sub>-out-CNT/PI system [45,46], while 2,4,6-TCP was partially removed (35.8%) under the same conditions. These results indicated that  $\text{IO}_3^{\bullet}$  might be involved in the degradation of organic compounds in the E/Fe<sub>2</sub>O<sub>3</sub>-out-CNT/PI system, which can be formed by reduction of  $\text{IO}_4^-$  at the surface of the Fe<sub>2</sub>O<sub>3</sub>-out-CNT cathode (Eq. (8)).

EPR-spin trapping was also used to directly verify essential ROS. No characteristic peaks were observed in the EPR spectra obtained from PI or CNT in the presence of DMPO (Fig. 4(b)). As expected, the characteristic quadrupole peak signals of DMPO-HO<sup>•</sup> (1:2:2:1) were observed in the E/Fe<sub>2</sub>O<sub>3</sub>-out-CNT/PI system. The intensity of the corresponding

signal from the E/Fe<sub>2</sub>O<sub>3</sub>-in-CNT/PI system was much weaker than that of E/Fe<sub>2</sub>O<sub>3</sub>-out-CNT/PI system, which agreed with the radical quenching tests. Noticeably, a 1:1:1 triplet signal of TEMP- $^1\text{O}_2$  was observed in all four systems in the absence of BPA, indicating the presence of  $^1\text{O}_2$  (Fig. 4(c)). Compared with other systems, the intensity signal of  $^1\text{O}_2$  was much greater in the E/Fe<sub>2</sub>O<sub>3</sub>-in-CNT/PI system. Besides, the lifetime of  $^1\text{O}_2$  in D<sub>2</sub>O (22–70  $\mu$ s) was 10-fold longer than that in H<sub>2</sub>O (2  $\mu$ s) [47]. Thereby, the EPR measurements of  $^1\text{O}_2$  were performed by replacing the ultrapure water as D<sub>2</sub>O. As observed in Fig. S15, the signal intensity of  $^1\text{O}_2$  was markedly increased when using D<sub>2</sub>O as the solvent, which provide another solid evidence on the  $^1\text{O}_2$  generation. The addition of FFA would significantly suppress the signal intensity of  $^1\text{O}_2$  (Fig. S16). Furthermore, the EPR spectra in the presence of 10 mM *p*-BQ (quenching agent of  $\text{O}_2^{\bullet-}$ ) leads to evidently weakened  $^1\text{O}_2$  signal intensity (Fig. S16), indicating  $\text{O}_2^{\bullet-}$  may be the key intermediate for the  $^1\text{O}_2$  generation. Here,  $^1\text{O}_2$  may arise from the recombination of  $\text{O}_2^{\bullet-}$ , generated as an intermediate from PI and oxygen [48]. To verify this hypothesis, a control experiment was conducted in deoxygenated condition obtained by pre-purging the BPA solution with N<sub>2</sub>. The results in Fig. S17 showed that BPA degradation efficiency was not affected by N<sub>2</sub> atmosphere, implying that the contribution of dissolved oxygen to BPA degradation was negligible. In addition, the EPR signal from TEMP- $^1\text{O}_2$  adduct in the E/Fe<sub>2</sub>O<sub>3</sub>-in-CNT/PI system was not suppressed under the N<sub>2</sub> purged environment (Fig. S18). This suggested that  $^1\text{O}_2$  was not derived from the dissolved oxygen.

A previous study demonstrated that the CNT-mediated electron transfer process played a dominant role toward the elimination of organic contaminants in CNT/PI system [49]. For the purpose of analyzing the electron transfer processes, linear sweep voltammetry (LSV) was performed to monitor the current response in both E/Fe<sub>2</sub>O<sub>3</sub>-out-CNT/PI and E/Fe<sub>2</sub>O<sub>3</sub>-in-CNT/PI systems. As shown in Fig. S19, both Fe<sub>2</sub>O<sub>3</sub>-out-CNT and Fe<sub>2</sub>O<sub>3</sub>-in-CNT filters showed no evident current increase in the existence of PI and BPA. This ruled out the possibility of an electron transfer process between BPA (electron donor) and PI (electron acceptor) in both systems.

To further compare the key ROS produced in confined and unconfined system, the concentrations of  $^1\text{O}_2$  and HO<sup>•</sup> were determined by using EPR method on a quantitative basis. As shown in Fig. 4(d), the HO<sup>•</sup> concentration of 6.6  $\mu\text{mmol/L}$  obtained for E/Fe<sub>2</sub>O<sub>3</sub>-out-CNT/PI system was 6.8 times higher than that of 0.98  $\mu\text{mmol/L}$  for E/Fe<sub>2</sub>O<sub>3</sub>-in-CNT/PI system. In comparison,  $^1\text{O}_2$  concentration (0.24  $\mu\text{mmol/L}$ ) was more than one order of magnitude lower than that of E/Fe<sub>2</sub>O<sub>3</sub>-in-CNT/PI system (18.2  $\mu\text{mmol/L}$ ). These results confirmed the dominance of different ROS in the E/Fe<sub>2</sub>O<sub>3</sub>-in-CNT/PI and E/Fe<sub>2</sub>O<sub>3</sub>-out-CNT/PI systems, possibly due to the contrasting interactions of Fe<sub>2</sub>O<sub>3</sub> with the interior/exterior CNT walls.

Based on these investigations, different working mechanisms were proposed for the unconfined and confined Fe<sub>2</sub>O<sub>3</sub> filter systems (Fig. 5). The results indicated that BPA degradation in the E/Fe<sub>2</sub>O<sub>3</sub>-out-CNT/PI system was a dual radical (HO<sup>•</sup> and  $\text{IO}_3^{\bullet}$ ) process, in which HO<sup>•</sup> accounted for the majority of the degradation process (58.5%). The following mechanism of PI activation was proposed: Fe(III) on the surface of E/Fe<sub>2</sub>O<sub>3</sub>-out-CNT filter cathode is reduced to Fe(II) (Eq. (4)); the interaction between Fe(II) and PI leads to HO<sup>•</sup> generation, similar with the Fenton reaction. This appeared to be quite similar as the single-electron-transfer reactions of  $\text{IO}_4^-$  photosensitization or zero-valence metals (e.g., Fe<sup>0</sup>-Cu and Fe<sup>0</sup>-Ni systems) [45,50,51],  $\text{IO}_3^{\bullet}$  is formed from the reduction of  $\text{IO}_4^-$  at the E/Fe<sub>2</sub>O<sub>3</sub>-out-CNT filter cathode (Eq. (8)).

In the E/Fe<sub>2</sub>O<sub>3</sub>-in-CNT/PI system,  $^1\text{O}_2$  was considered as the dominant ROS for BPA degradation and the following mechanism was proposed: i) Fe(III) was rapidly reduced to Fe(II) in the presence of an electric field (Eq. (4)), which then participates in the activation of PI to produce  $\text{O}_2^{\bullet-}$  (Eq. (5)). It is speculated that the nanoconfinement changes the PI activation pathways both kinetically and thermodynamically [52]. When compared with nonconfined Fe<sub>2</sub>O<sub>3</sub> nanoparticles,

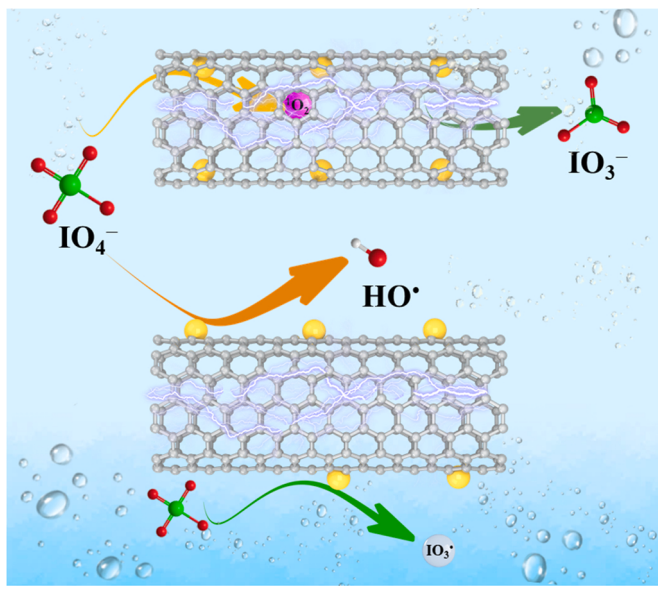


**Fig. 5.** A schematic illustration of possible mechanism of pollutants degradation in E/Fe<sub>2</sub>O<sub>3</sub>-in-CNT/PI and E/Fe<sub>2</sub>O<sub>3</sub>-out-CNT/PI systems.

such nanoconfinement by CNT poses a strong electronic interaction between the electron-deficient CNT concave surface and those encapsulated Fe<sub>2</sub>O<sub>3</sub> particles [24,28]. ii) <sup>1</sup>O<sub>2</sub> was produced via the recombination of O<sub>2</sub><sup>•-</sup> (Eq. (6)) or the reaction of IO<sub>4</sub><sup>-</sup> with O<sub>2</sub><sup>•-</sup> (Eq. (7)). To gain further insights into the mechanism of PI conversion, the decomposition of IO<sub>4</sub><sup>-</sup> was followed after activation in the E/Fe<sub>2</sub>O<sub>3</sub>-in-CNT/PI system in the presence and absence of BPA (Fig. S20). In the absence of BPA, only a small fraction of PI (17.5%) was decomposed by the E/Fe<sub>2</sub>O<sub>3</sub>-in-CNT filter. In contrast, such fraction increased significantly to 77.2% in the presence of BPA. This phenomenon could be explained from the perspective of chemical reaction equilibrium. The presence of BPA consistently consumed the as-produced <sup>1</sup>O<sub>2</sub>, leading to the proceed in the forward direction of Eqs. (5)–(7) as well as an enhanced IO<sub>4</sub><sup>-</sup> decomposition efficiency compared with that in the absence of BPA. The reduction of IO<sub>4</sub><sup>-</sup> was accompanied by the stoichiometric formation of IO<sub>3</sub><sup>-</sup>, and the overall concentration of iodine remained in balance. Additionally, replacing IO<sub>4</sub><sup>-</sup> by IO<sub>3</sub><sup>-</sup> led to no removal of BPA (Fig. S21). Note that IO<sub>3</sub><sup>-</sup> was the major product of IO<sub>4</sub><sup>-</sup> reduction, as no iodine species, or reduction to I<sup>-</sup>, occurred in the system. Specifically, the possible generation of I<sub>2</sub>/I<sub>3</sub><sup>-</sup> and HOI could be excluded based on the results obtained using starch chromatometry and phenol as a capturing reagent [53,54], respectively (Text S3, Figs. S22 and S23).

#### 3.4. Theoretical calculations

DFT calculations were conducted to gain a deeper insight into the confinement effect on PI activation. The results showed that the formation of Fe<sub>2</sub>O<sub>3</sub>-CNT complexes in both Fe<sub>2</sub>O<sub>3</sub>-out-CNT and Fe<sub>2</sub>O<sub>3</sub>-in-CNT filters were thermodynamically stable. Fig. 6 shows that PI could be adsorbed onto the surface of Fe<sub>2</sub>O<sub>3</sub>-out-CNT at distances between the Fe atom and each of the two O atoms of PI of 2.10 and 2.09 angstrom, respectively. In comparison, PI could be directly decomposed in the Fe<sub>2</sub>O<sub>3</sub>-in-CNT, instead of the formation of a stable adsorption complex. In viewpoint of thermodynamics, the direct decomposition of PI in the Fe<sub>2</sub>O<sub>3</sub>-in-CNT was 54.3 kcal/mol more favorable than adsorption on the surface of Fe<sub>2</sub>O<sub>3</sub>-out-CNT. Hence, the DFT calculations suggested that the confinement effect of the Fe<sub>2</sub>O<sub>3</sub>-in-CNT was important in PI activation, which supported the experimental observations.

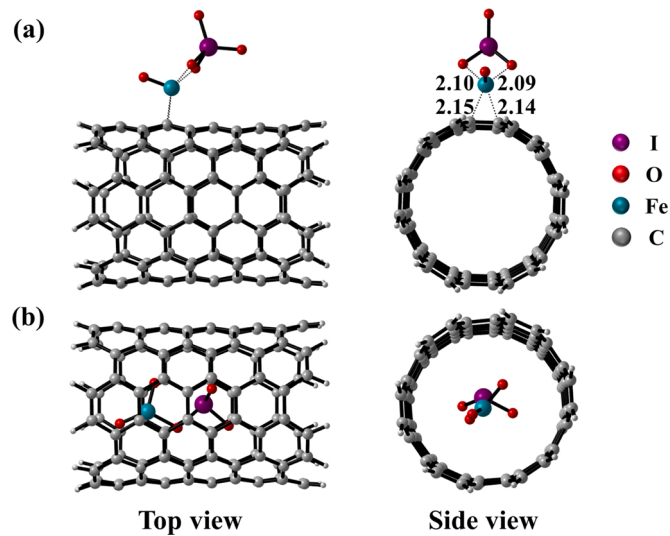


**Fig. 6.** DFT-optimized geometries of (a) Fe<sub>2</sub>O<sub>3</sub>-out-CNT and (b) Fe<sub>2</sub>O<sub>3</sub>-in-CNT with PI.

#### 3.5. BPA degradation pathways

Identification of the BPA degradation intermediates was an important step in understanding the mineralization mechanism. Fig. S24 shows the key intermediates detected by LC-MS in the E/Fe<sub>2</sub>O<sub>3</sub>-in-CNT/PI degradation system of BPA. Seven degradation intermediates were identified with *m/z* values of 244, 260, 266, 238, 192, 176, and 214 amu.

The Fukui index based on natural population charge (Text S4) was used to predict the active sites of BPA (Fig. S25(a) and (b)). As the main active species, <sup>1</sup>O<sub>2</sub> was classified as an attacking nucleophile, *i.e.*, it favored sites that could readily lose an electron. Hence, the Fukui index (*f*<sup>+</sup>) was used to determine the potential electrophilic sites of BPA and the distribution of *f*<sup>+</sup> is illustrated in Fig. S25(c). C15 (*f*<sup>+</sup> = 0.0656) and C25 (*f*<sup>+</sup> = 0.0652) gave the highest Fukui indices, indicating the most active sites on BPA. Based on these values and the molecular weights of the detected intermediates, degradation pathways for BPA (228 amu) were proposed (Fig. 7). In pathway I, oxidation of the benzene ring from the nucleophilic addition of <sup>1</sup>O<sub>2</sub> at the C15 and C25 active sites leads to the formation of products A (244 amu; single oxygen atom) and B (260 amu; two oxygen atoms). Following ring-opening, product C (266 amu) is formed, from which products D (238 amu) and E (192 amu) are formed C (266 amu) by oxidation. Cleavage of the C–C bond of product E (192 amu) led to the formation of F (176 amu). In pathway II, product G (214 amu) was obtained from the demethylation of BPA (228 amu). Finally, all the above intermediates could be degraded into smaller molecules (*e.g.*, carboxylic acids) and further mineralized to CO<sub>2</sub> and H<sub>2</sub>O.

#### 3.6. Evaluation of practical applications

##### 3.6.1. Effect of water chemistry

Due to the high specificity of <sup>1</sup>O<sub>2</sub> towards BPA, it was inferred that the E/Fe<sub>2</sub>O<sub>3</sub>-in-CNT/PI system might exhibit high selectivity towards the pollutant in complex aqueous matrices. Hence, the impacts of inorganic constituents and natural organic matters (*e.g.*, humic acid, HA) on the degradation of BPA were investigated. As expected, the presence of these materials had a negligible influence on the degradation of BPA (Fig. S26(a)). The efficacy of the E/Fe<sub>2</sub>O<sub>3</sub>-in-CNT/PI system was also evaluated using tap water and the lake water (Fig. S26(b)). The results showed that BPA degradation efficiencies of 94.3% and 81.8% could be achieved in spiked tap water and lake water respectively. This indicated effectiveness and reliability of the E/Fe<sub>2</sub>O<sub>3</sub>-in-CNT/PI system for practical applications.

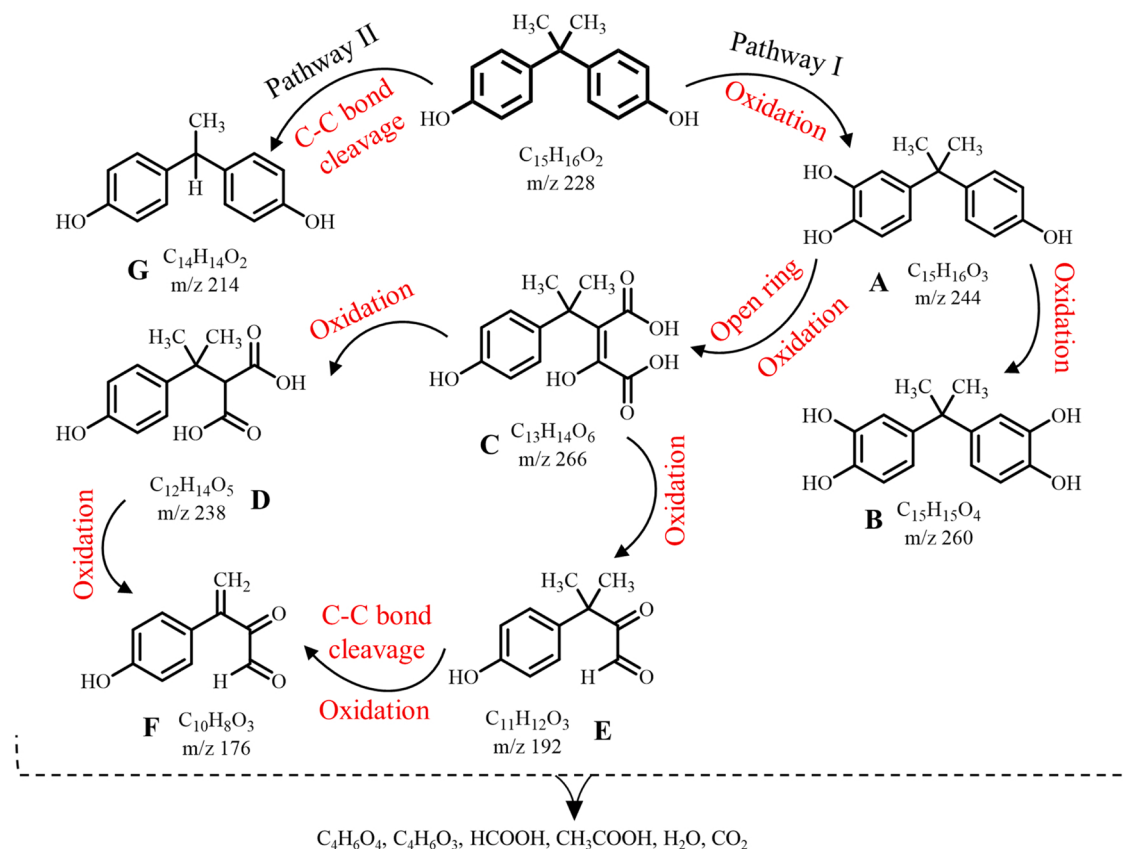


Fig. 7. Possible degradation pathways of BPA in the E/Fe<sub>2</sub>O<sub>3</sub>-in-CNT/PI system.

### 3.6.2. Stability evaluation

Long-term continuous operation (48 h) in the single-pass mode showed a small reduction (8.9%) in BPA removal efficiency for the Fe<sub>2</sub>O<sub>3</sub>-in-CNT functional filter (Fig. 8(a)), while that of E/Fe<sub>2</sub>O<sub>3</sub>-out-CNT/PI was much greater (35.5% after 48 h operation). The difference in performance was attributed to the reduced loss of Fe in the E/Fe<sub>2</sub>O<sub>3</sub>-in-CNT/PI system (< 10 µg/L) compared with the E/Fe<sub>2</sub>O<sub>3</sub>-out-CNT/PI system (316.5 µg/L) during operation (Fig. 8(b)). The differences in Fe loss could be due to confinement of Fe<sub>2</sub>O<sub>3</sub> within the interior cavity of CNT of the E/Fe<sub>2</sub>O<sub>3</sub>-in-CNT/PI system, which minimizes corrosion and

leaching.

### 3.6.3. Energy consumption

Practical wastewater treatments usually require efficient energy utilization [55–57]. Notably, the energy consumption (0.05 kWh/m<sup>3</sup>) of the E/Fe<sub>2</sub>O<sub>3</sub>-in-CNT/PI system under optimized conditions (*i.e.*, applied voltage, -1.5 V; electric current, 2.0 mA; flow rate, 1.0 mL/min) (Text S5) was much lower than other electrochemical processes reported in literatures [58–61]. Such low energy consumption could also be associated with the convection-enhanced mass transport, improved catalyst

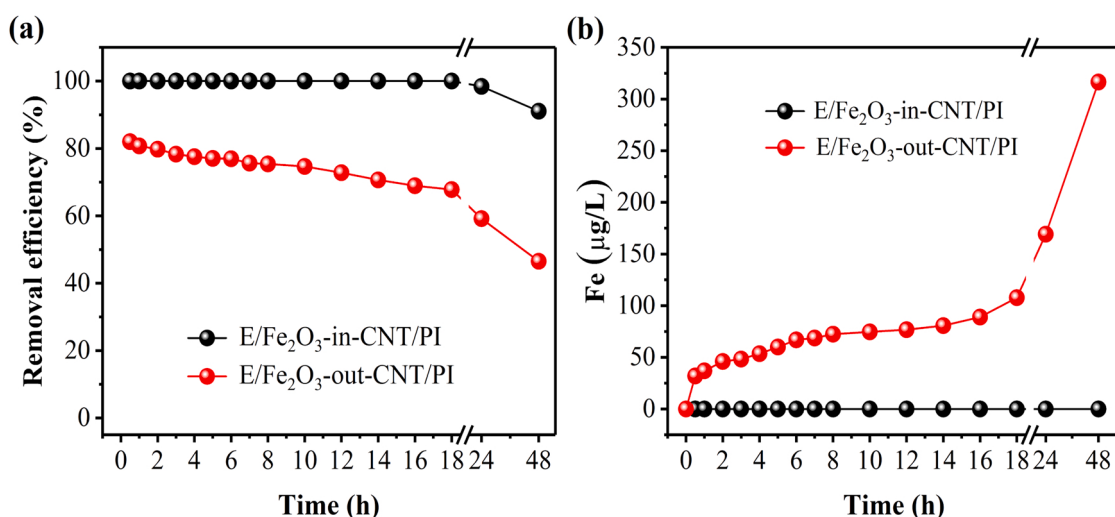


Fig. 8. Evaluation of (a) the long-term stability and (b) Fe leaching of the E/Fe<sub>2</sub>O<sub>3</sub>-in-CNT/PI and E/Fe<sub>2</sub>O<sub>3</sub>-out-CNT/PI systems, respectively. Experimental conditions:  $[BPA]_0 = 0.022$  mM,  $[PI]_0 = 2.0$  mM,  $[pH]_0 = 5.7$ , voltage = -1.5 V, and flow rate = 1.0 mL/min.

stability, abundant catalytic active sites [62,63] as well as the synergistic effects between electric field and nanoconfined effect.

#### 4. Conclusions

A novel electrochemical PI activation system was developed for the ultrafast and robust degradation of micropollutants. Compared with the radical-dominated pathway observed for the E/Fe<sub>2</sub>O<sub>3</sub>-out-CNT/PI system, a nonradical-process dominated the E/Fe<sub>2</sub>O<sub>3</sub>-in-CNT/PI system. The E/Fe<sub>2</sub>O<sub>3</sub>-in-CNT/PI system demonstrated superior performance over the E/Fe<sub>2</sub>O<sub>3</sub>-out-CNT/PI system for the degradation of BPA over a wide pH range. BPA removal efficiency of > 90% could be sustained over 48 h operation, suggesting that the Fe<sub>2</sub>O<sub>3</sub>-in-CNT filter had good stability and reactivity. The results from this study provide further insight into the mechanisms of heterogeneous electrochemistry-mediated PI activation. They may also provide a platform to develop efficient, sustainable, and economical technologies for future water remediation applications.

#### CRediT authorship contribution statement

**Dongli Guo:** Data curation, Methodology, Investigation, Writing – original draft. **Yuan Yao:** Formal analysis, Software, DFT calculation. **Shijie You:** Writing – review & editing, Project administration, Resources. **Limin Jin:** Methodology, Validation. **Ping Lu:** Characterization. **Yanbiao Liu:** Conceptualization, Writing – review & editing, Supervision.

#### Declaration of Competing Interest

The authors declare that they have no known competing financial interests or personal relationships that could have appeared to influence the work reported in this paper.

#### Acknowledgments

This work was supported by the National Natural Science Foundation of China (No. 52170068), the Fundamental Research Funds for the Central Universities and Graduate Student Innovation Fund of Donghua University (CUSF-DH-D-2021038).

#### Appendix A. Supplementary material

Supplementary data associated with this article can be found in the online version at [doi:10.1016/j.apcatb.2022.121289](https://doi.org/10.1016/j.apcatb.2022.121289).

#### References

- M. Patel, R. Kumar, K. Kishor, T. Mlsna, C.U. Pittman, D. Mohan, Pharmaceuticals of emerging concern in aquatic systems: chemistry, occurrence, effects, and removal methods, *Chem. Rev.* 119 (2019) 3510–3673.
- Y. Xu, T.J. Liu, Y. Zhang, F. Ge, R.M. Steel, L.Y. Sun, Advances in technologies for pharmaceuticals and personal care products removal, *J. Mater. Chem. A* 5 (2017) 12001–12014.
- R.P. Schwarzenbach, B.I. Escher, K. Fenner, T.B. Hofstetter, C.A. Johnson, U. von Gunten, B. Wehrli, The challenge of micropollutants in aquatic systems, *Science* 313 (2006) 1072–1077.
- C. Grandclement, I. Seysiecq, A. Piram, P. Wong-Wah-Chung, G. Vanot, N. Tiliacos, N. Roche, P. Doumenc, From the conventional biological wastewater treatment to hybrid processes, the evaluation of organic micropollutant removal: a review, *Water Res.* 111 (2017) 297–317.
- K. Arola, H. Hatakka, M. Manttari, M. Kallioinen, Novel process concept alternatives for improved removal of micropollutants in wastewater treatment, *Sep. Purif. Technol.* 186 (2017) 333–341.
- A. Alsbaei, B.J. Smith, L. Xiao, Y. Ling, D.E. Helbling, W.R. Dichtel, Rapid removal of organic micropollutants from water by a porous  $\beta$ -cyclodextrin polymer, *Nature* 529 (2016) 190–194.
- Y. Zong, Y.F. Shao, Y.Q. Zeng, B.B. Shao, L.Q. Xu, Z.Y. Zhao, W. Liu, D.L. Wu, Enhanced oxidation of organic contaminants by iron(II)-activated periodate: the significance of high-valent iron-oxo species, *Environ. Sci. Technol.* 55 (2021) 7634–7642.
- H.W. Sun, F. He, W. Choi, Production of reactive oxygen species by the reaction of periodate and hydroxylamine for rapid removal of organic pollutants and waterborne bacteria, *Environ. Sci. Technol.* 54 (2020) 6427–6437.
- E.T. Yun, H.Y. Yoo, W. Kim, H.E. Kim, G. Kang, H. Lee, S. Lee, T. Park, C. Lee, J. H. Kim, J. Lee, Suppressing polysulfide dissolution via cohesive forces by interwoven carbon nanofibers for high-areal-capacity lithium-sulfur batteries, *Appl. Catal. B* 203 (2017) 475–484.
- Y.N. Shang, X. Xu, Q.Y. Yue, B.Y. Gao, Y.W. Li, Nitrogen-doped carbon nanotubes encapsulating Fe/Zn nanoparticles as a persulfate activator for sulfamethoxazole degradation: role of encapsulated bimetallic nanoparticles and nonradical reaction, *Environ. Sci. Nano* 7 (2020) 1444–1453.
- J.B. Wang, S.Z. Li, Q.Y. Qin, C. Peng, Sustainable and feasible reagent-free electro-Fenton via sequential dual-cathode electrocatalysis, *Proc. Natl. Acad. Sci. USA* 118 (2021), e2108573118.
- X. Zhang, X.B. Yu, X.Y. Yu, M. Kamali, L. Appels, B. Van der Bruggen, D. Cabooter, R. Dewil, Efficiency and mechanism of 2,4-dichlorophenol degradation by the UV/IO<sub>4</sub><sup>-</sup> process, *Sci. Total Environ.* 782 (2021), 146781.
- Y.X. Wang, Z.M. Ao, H.Q. Sun, X.G. Duan, S.B. Wang, Activation of peroxymonosulfate by carbonaceous oxygen groups: experimental and density functional theory calculations, *Appl. Catal. B* 198 (2016) 295–302.
- Z.Z. Li, C.S. Shen, Y.B. Liu, C.Y. Ma, F. Li, B. Yang, M.H. Huang, Z.W. Wang, L. M. Dong, W. Sand, Carbon nanotube filter functionalized with iron oxychloride for flow-through electro-Fenton, *Appl. Catal. B* 260 (2020), 118204.
- A.D. Bokare, W. Choi, Singlet-oxygen generation in alkaline periodate solution, *Environ. Sci. Technol.* 49 (2015) 14392–14400.
- J.K. Du, G.F. Xiao, Y.X. Xi, X.W. Zhu, F. Su, S.H. Kim, Periodate activation with manganese oxides for sulfanilamide degradation, *Water Res.* 169 (2020), 115278.
- Y.C. Lee, M.J. Chen, C.P. Huang, J. Kuo, S.L. Lo, Efficient sonochemical degradation of perfluoroctanoic acid using periodate, *Ultrason. Sonochem.* 31 (2016) 499–505.
- Y.J. Li, H.R. Dong, L. Li, L. Tang, R. Tian, R. Li, J. Chen, Q.Q. Xie, Z. Jin, J.Y. Xiao, S.J. Xiao, G.M. Zeng, Recent advances in waste water treatment through transition metal sulfides-based advanced oxidation processes, *Water Res.* 192 (2021), 116850.
- Y.J. Yao, H. Chen, J.C. Qin, G.D. Wu, C. Lian, J. Zhang, S.B. Wang, Iron encapsulated in boron and nitrogen codoped carbon nanotubes as synergistic catalysts for Fenton-like reaction, *Water Res.* 101 (2016) 281–291.
- L. He, C. Yang, J. Ding, M.Y. Lu, C.X. Chen, G.Y. Wang, J.Q. Jiang, L. Ding, G.S. Liu, N.Q. Ren, S.S. Yang, Fe, N-doped carbonaceous catalyst activating periodate for micropollutant removal: significant role of electron transfer, *Appl. Catal. B* 303 (2022), 120880.
- Y. Zong, Y.F. Shao, W.J. Ji, Y.Q. Zeng, L.Q. Xu, D.L. Wu, Surface-mediated periodate activation by nano zero-valent iron for the enhanced abatement of organic contaminants, *J. Hazard. Mater.* 423 (2022), 126991.
- Y. Chen, G. Zhang, H.J. Liu, J.H. Qu, Confining free radicals in close vicinity to contaminants enables ultrafast fenton-like processes in the interspacing of MoS<sub>2</sub> membranes, *Angew. Chem. Int. Ed.* 58 (2019) 8134–8138.
- P. Su, M.H. Zhou, G.B. Ren, X.Y. Lu, X.D. Du, G. Song, A carbon nanotube-confined iron modified cathode with prominent stability and activity for heterogeneous electro-Fenton reactions, *J. Mater. Chem. A* 7 (2019) 24408–24419.
- Z.C. Yang, J.S. Qian, A.Q. Yu, B.C. Pan, Singlet oxygen mediated iron-based Fenton-like catalysis under nanoconfinement, *Proc. Natl. Acad. Sci. USA* 116 (2019) 6659–6664.
- D.L. Guo, Y.B. Liu, H.D. Ji, C.C. Wang, B. Chen, C.S. Shen, F. Li, Y.X. Wang, P. Lu, W. Liu, Silicate-enhanced heterogeneous flow-through electro-fenton system using iron oxides under nanoconfinement, *Environ. Sci. Technol.* 55 (2021) 4045–4053.
- Y.B. Liu, F.Q. Liu, N. Ding, X.M. Hu, C.S. Shen, F. Li, M.H. Huang, Z.W. Wang, W. Sand, C.C. Wang, Recent advances on electroactive CNT-based membranes for environmental applications: the perfect match of electrochemistry and membrane separation, *Chin. Chem. Lett.* 31 (2020) 2539–2548.
- D.R. Kearns, Physical and chemical properties of singlet molecular oxygen, *Chem. Rev.* 71 (1971) 395–427.
- W. Chen, X.L. Pan, X.H. Bao, Tuning of redox properties of iron and iron oxides via encapsulation within carbon nanotubes, *J. Am. Chem. Soc.* 129 (2007) 7421–7426.
- M.J. Frisch, G.W. Trucks, H.B. Schlegel, G.E. Scuseria, M.A. Robb, J.R. Cheeseman, G. Scalmani, V. Barone, B. Mennucci, G.A. Petersson, Gaussian, Inc., Wallingford CT, 2009.
- W. Chen, Z.L. Fan, X.L. Pan, X.H. Bao, Effect of confinement in carbon nanotubes on the activity of Fischer-Tropsch iron catalyst, *J. Am. Chem. Soc.* 130 (2008) 9414–9419.
- C.F. Wang, S.J. Guo, X.L. Pan, W. Chen, X.H. Bao, Tailored cutting of carbon nanotubes and controlled dispersion of metal nanoparticles inside their channels, *J. Mater. Chem.* 18 (2008) 5782–5786.
- G.X. Zhu, W. Zhu, Y. Lou, J. Ma, W.Q. Yao, R.L. Zong, Y.F. Zhu, Encapsulate  $\alpha$ -MnO<sub>2</sub> nanofiber within graphene layer to tune surface electronic structure for efficient ozone decomposition, *Nat. Commun.* 12 (2021) 4152.
- S. Chen, J.W. Zhu, X.D. Wu, Q.F. Han, X. Wang, Graphene oxide–MnO<sub>2</sub> nanocomposites for supercapacitors, *ACS Nano* 4 (2010) 2822–2830.
- L.J. Zhong, C. Frandsen, S. Mørup, Y. Hu, C. Pan, L.N. Cleemann, J.O. Jensen, Q. F. Li, <sup>57</sup>Fe-Mössbauer spectroscopy and electrochemical activities of graphitic layer encapsulated iron electrocatalysts for the oxygen reduction reaction, *Appl. Catal. B* 221 (2018) 406–412.
- M. Menon, A.N. Andriots, G.E. Froudakis, Curvature dependence of the metal catalyst atom interaction with carbon nanotubes walls, *Chem. Phys. Lett.* 320 (2000) 425–434.

[36] W. Chen, Z.L. Fan, B. Zhang, G.J. Ma, K. Takanabe, X.X. Zhang, Z.P. Lai, Enhanced visible-light activity of titania via confinement inside carbon nanotubes, *J. Am. Chem. Soc.* 133 (2011) 14896–14899.

[37] X. Cheng, H.G. Guo, Y.L. Zhang, X. Wu, Y. Liu, Non-photochemical production of singlet oxygen via activation of persulfate by carbon nanotubes, *Water Res.* 113 (2017) 80–88.

[38] Q.Y. Yi, J.H. Ji, B. Shen, C.C. Dong, J. Liu, J.L. Zhang, M.Y. Xing, Singlet oxygen triggered by superoxide radicals in a molybdenum cocatalytic fenton reaction with enhanced REDOX activity in the environment, *Environ. Sci. Technol.* 53 (2019) 9725–9733.

[39] Z.Y. Feng, Q.L. Tian, Q.Q. Yang, Y.B. Zhou, H.Y. Zhao, G.H. Zhao, Selectively photoelectrocatalytic reduction of oxygen to hydroxyl radical and singlet oxygen: mechanism and validation in coal wastewater, *Appl. Catal. B* 286 (2021), 119908.

[40] Y.J. Choi, H.I. Yoon, C.H. Lee, Lu Vetrakova, D. Heger, K. Kim, J. Kim, Activation of periodate by freezing for the degradation of aqueous organic pollutants, *Environ. Sci. Technol.* 52 (2018) 5378–5385.

[41] S.S. Zhu, X.J. Li, J. Kang, X.G. Duan, S.B. Wang, Persulfate activation on crystallographic manganese oxides: mechanism of singlet oxygen evolution for nonradical selective degradation of aqueous contaminants, *Environ. Sci. Technol.* 53 (2019) 307–315.

[42] C.Y. Chen, C.T. Jafvert, Photoreactivity of carboxylated single-walled carbon nanotubes in sunlight: reactive oxygen species production in water, *Environ. Sci. Technol.* 44 (2010) 6674–6679.

[43] X.W. Li, J. Ma, Y.F. Gao, X.T. Liu, Y. Wei, Z.J. Liang, Enhanced atrazine degradation in the Fe(III)/peroxymonosulfate system via accelerating Fe(II) regeneration by benzoquinone, *Chem. Eng. J.* 427 (2022), 131995.

[44] Y. Chen, C.J. Miller, T.D. Waite, pH dependence of hydroxyl radical, ferryl, and/or ferric peroxy species generation in the heterogeneous fenton process, *Environ. Sci. Technol.* 56 (2022) 1278–1288.

[45] H. Lee, H.Y. Yoo, J. Choi, I.H. Nam, S. Lee, S. Lee, J.H. Kim, C. Lee, J. Lee, Oxidizing capacity of periodate activated with iron-based bimetallic nanoparticles, *Environ. Sci. Technol.* 48 (2014) 8086–8093.

[46] N.E. Chadi, S. Merouani, O. Hamdaoui, M. Bouhelassa, M. Ashokkumar, H<sub>2</sub>O<sub>2</sub>/periodate (IO<sub>4</sub><sup>-</sup>): a novel advanced oxidation technology for the degradation of refractory organic pollutants, *Environ. Sci. Water Res. Technol.* 5 (2019) 1113–1123.

[47] A. Gorman, M. Rodgers, Singlet molecular oxygen, *Chem. Soc. Rev.* 10 (1981) 205–231.

[48] O. Hamdaoui, S. Merouani, Improvement of sonochemical degradation of Brilliant blue R in water using periodate ions: implication of iodine radicals in the oxidation process, *Ultrason. Sonochem.* 37 (2017) 344–350.

[49] E.T. Yun, H.Y. Yoo, H. Bae, H.I. Kim, J. Lee, Exploring the role of persulfate in the activation process: radical precursor versus electron acceptor, *Environ. Sci. Technol.* 51 (2017) 10090–10099.

[50] L.H. Chia, X.M. Tang, L.K. Weavers, Kinetics and mechanism of photoactivated periodate reaction with 4-chlorophenol in acidic solution, *Environ. Sci. Technol.* 38 (2004) 6875–6880.

[51] M.H. Cao, B.B. Wang, H.S. Yu, L.L. Wang, S.H. Yuan, J. Chen, Photochemical decomposition of perfluorooctanoic acid in aqueous periodate with VUV and UV light irradiation, *J. Hazard. Mater.* 179 (2010) 1143–1146.

[52] J.S. Qian, X. Gao, B.C. Pan, Nanoconfinement-mediated water treatment: from fundamental to application, *Environ. Sci. Technol.* 54 (2020) 8509–8526.

[53] Y. Feng, P.H. Lee, D.L. Wu, K. Shih, Rapid selective circumneutral degradation of phenolic pollutants using peroxyomonosulfate-iodide metal-free oxidation: role of iodine atoms, *Environ. Sci. Technol.* 51 (2017) 2312–2320.

[54] J. Li, J. Jiang, Y. Zhou, S.Y. Pang, Y. Gao, C.C. Jiang, J. Ma, Y.X. Jin, Y. Yang, G. Q. Liu, L.H. Wang, C.T. Guan, Kinetics of oxidation of iodide (I<sup>-</sup>) and hypoiodous acid (HOI) by peroxyomonosulfate (PMS) and formation of iodinated products in the PMS/T/NOM system, *Environ. Sci. Technol. Lett.* 4 (2017) 76–82.

[55] X.B. Zhu, D. Jassby, Electroactive membranes for water treatment: enhanced treatment functionalities, energy considerations, and future challenges, *Acc. Chem. Res.* 52 (2019) 1177–1186.

[56] B.P. Chaplin, The prospect of electrochemical technologies advancing worldwide water treatment, *Acc. Chem. Res.* 52 (2019) 596–604.

[57] Y.B. Liu, G.D. Gao, C.D. Vecitis, Prospects of an electroactive carbon nanotube membrane toward environmental applications, *Acc. Chem. Res.* 53 (2020) 2892–2902.

[58] T.X.H. Le, H. Haflrich, A.D. Shah, B.P. Chaplin, Energy-efficient electrochemical oxidation of perfluoroalkyl substances using a Ti4O7 reactive electrochemical membrane anode, *Environ. Sci. Technol. Lett.* 6 (2019) 504–510.

[59] J.C. Sun, Q.Y. Wang, J. Zhang, Z.W. Wang, Z.C. Wu, Degradation of sulfadiazine in drinking water by a cathodic electrochemical membrane filtration process, *Electrochim. Acta* 277 (2018) 77–87.

[60] J.J. Zheng, J.X. Ma, Z.W. Wang, S.P. Xu, T.D. Waite, Z.C. Wu, Contaminant removal from source waters using cathodic electrochemical membrane filtration: mechanisms and implications, *Environ. Sci. Technol.* 51 (2017) 2757–2765.

[61] W.Y. Duan, G.D. Chen, C.X. Chen, R. Sanghvi, A. Iddya, S. Walker, H.Z. Liu, A. Ronen, D. Jassby, Electrochemical removal of hexavalent chromium using electrically conducting carbon nanotube/polymer composite ultrafiltration membranes, *J. Membr. Sci.* 531 (2017) 160–171.

[62] Y.M. Zhao, M. Sun, X.X. Wang, C. Wang, D.W. Lu, W. Ma, S.A. Kube, J. Ma, M. Elimelech, Janus electrocatalytic flow-through membrane enables highly selective singlet oxygen production, *Nat. Commun.* 11 (2020) 6228–6237.

[63] X.Y. Ni, H. Liu, C. Wang, W.L. Wang, Z.B. Xu, Z. Chen, Y.H. Wu, H.Y. Hu, Comparison of carbonized and graphitized carbon fiber electrodes under flow-through electrode system (FES) for high-efficiency bacterial inactivation, *Water Res.* 168 (2020), 115150.